

Characterization of Li-Doped MgO Catalysts for Oxidative Coupling of Methane by Means of Mg K-Edge XANES

Hirofumi Aritani,* Hiroyuki Yamada, Takashi Nishio, Takeshi Shiono, and Seiichiro Imamura

Faculty of Engineering and Design, Kyoto Institute of Technology, Sakyo, Kyoto 606-8585, Japan

Masataka Kudo

Criminal Investigation Laboratory, Metropolitan Police Department, Chiyoda, Tokyo 100-690, Japan

Sadao Hasegawa

Department of Chemistry, Faculty of Education, Tokyo Gakugei University, Koganei, Tokyo 184-8501, Japan

Tsunehiro Tanaka and Satoshiro Yoshida

Division of Molecular Engineering, Graduate School of Engineering, Kyoto University, Sakyo, Kyoto 606-8501, Japan

Received: January 24, 2000; In Final Form: July 31, 2000

To characterize active defect sites in the near-surface and bulk phase of MgO in Li-doped MgO, structural analyses were carried out by means of XRD, XPS, Mg K-edge XANES, and SEM techniques. For Li–MgO calcined at 873 K, Li doping at a low content (2.5 wt % as Li) brings about the formation of defect species only in the near-surface, which is due to the localization of doped Li ions in the surface. In this case, the catalytic species containing a $\text{Li}^+ - \text{O}^-$ center exists in the surface region. At higher contents of more than 7.5 wt %, Li ions penetrate the MgO bulk, and its crystallinity decreases. The defect species possibly exist in the bulk phase. After oxidative coupling of methane reaction, the defect species are formed in the near-surface over MgO and Li–MgO. However, the C_2 selectivity is much higher on Li–MgO than on MgO. It is concluded that the defect species containing $\text{Li}^+ - \text{O}^-$ in both surface and bulk can act as the active species for producing C_2 compounds with high selectivity.

Introduction

Several reviews of the catalytically oxidative coupling of methane (OCM) have been published since the 1980s.^{1–6} Li-doped MgO is one of the typical catalysts for OCM and has been studied by many workers because of its high reactivity and C_2 selectivity.⁷ It is accepted widely that the catalytic activity for OCM is strongly related to the unique oxygen-anion species (e.g., O^- , O_2^{2-} , O_2^- , etc.) promoted by Li-doping.^{8,9} These oxygen species were characterized mainly by means of ESR. It was concluded by Lunsford et al. that $\text{Li}^+ - \text{O}^-$ centers in/on Li–MgO, which are in equilibrium with surface O^- centers via hole transport, play an important role for the activation of CH_4 .^{3,10,11} However, direct observation of the $\text{Li}^+ - \text{O}^-$ center is difficult because it is present at high temperatures and forms only in an O_2 atmosphere.¹² In the case of other alkali-doped MgO catalysts, the O^- species is also active, as reported by many workers.^{13–15} However, different oxygen species were proposed as active centers on other OCM catalysts. Otsuka et al. suggested that a peroxide anion, O_2^{2-} , acts as an active species on Sm_2O_3 or Na_2O_2 .^{16–18} It is reported that O_2^- anion possibly acts as the active species on La_2O_3 .^{19,20} As mentioned above, consistent active species for OCM reaction have not been agreed upon. In fact, it would be difficult to characterize the active oxygen species under the reaction conditions, and spectroscopic evidence may be available in the limited number of cases.²¹ On the other hand, MgO contains a small number of

various defect sites including vacancies, ionic impurities, and trapped charge carriers. Voskresenskaya et al. summarized that the formation of active oxygen anions for OCM is based on the activation of oxidants by structural defects.⁵ By Li-doping, the defect sites increase on MgO not only in the surface region but also in the bulk phase. The proposed mechanism of active center formation ($\text{Li}^+ - \text{O}^-$ sites and vacant holes)⁷ correlates with the formation of defect sites in both surface and bulk. For instance, Aika et al.^{22,23} studied the behavior of O^- sites by means of electron conductivity, and showed that hydrogen observed from hydroxyl groups in bulk defects can be assumed to form O^- (hole with O_2^-). As described above, the characterization of Li–MgO in both surface and bulk is important for elucidation of the defect site formation as the catalytic active species. However, direct spectroscopic observation of the defect sites is difficult. ESR is only available for characterization of “ESR-active” oxygen anions. Although XRD is available for characterizing the bulk phase of Li–MgO, crystallinity of the MgO can only be evaluated. More information about the active defect sites on Li–MgO is needed. In this work, we have applied Mg K-edge XANES for the characterization of the local structure around Mg^{2+} ions in the near-surface region. XANES at the Mg K-edge is sensitive to the symmetry around the Mg^{2+} ions and reflects not only cubic MgO but also “XRD-amorphous” phases. Therefore, structural information of all Mg^{2+} ions can be obtained. For XANES measurement, the total-

electron-yield mode was used. In this method, the penetration range of XANES is less than 38 nm because the electron yield is mainly due to low-energy secondary electrons, which are more abundant than *KLL*-Auger electrons and direct photoelectrons.^{24,25} The structural information obtained by XANES is associated with the “near-surface region”. Making a comparison between XANES and XRD results, the formation of vacancy sites and the crystallinity of MgO can be discussed in both the surface region and the bulk phase. By using these techniques, structural differences between surface and bulk have been discussed by Yoshida et al.^{26,27} We suggested in a previous report²⁸ that structural change of MgO in the near-surface is brought about at a low Li-doping content of about 2.5 wt %. In this study, we provide more detailed information on the structure of Li–MgO catalysts with various amounts of Li in both the bulk and near-surface by means of XANES, XRD, SEM, and XPS. In addition, the catalyst samples after OCM reaction are also characterized to compare with their structure before reaction.

Experimental Section

Preparation of Catalyst Samples. A MgO sample was obtained by calcination of Mg(OH)₂ (Kojundo-Kagaku Kenkyusho Co.; 99.9% Mg(OH)₂, contained impurities are Zn (40 ppm), Mn, Al (20 ppm), Cu, Fe, and Ca (less than 10 ppm)) at 873 K for 3 h followed by cooling to ambient temperature overnight. Li-doped MgO samples were prepared by impregnation of Mg(OH)₂ with an aqueous solution of LiNO₃ (Nacalai Tesque Co., Guaranteed reagent) at 343 K, and then excess water was evaporated at 343 K to form a paste. The paste was then dried at 353 K overnight and calcined at 873 K for 3 h.

Characterization of Catalyst Samples. The Mg *K*-edge XAFS (XANES and EXAFS) spectra were collected on BL-7A station^{29,30} of the soft X-ray beam line at UVSOR facility, in the Institute for Molecular Science, Okazaki, Japan (with a ring energy of 750 MeV and stored current of 120–220 mA). Each sample was mounted on carbon tape and then attached to a beryllium–copper dynode as the first-stage of the electron multiplier placed in a vacuum chamber. After the chamber had been evacuated ($<2.0 \times 10^{-7}$ Torr), the spectrum was measured in the total-electron-yield mode at room temperature, using a beryl double-crystal monochromator ($2d = 1.5965$ nm). The beam size at the sample was about 1.0×5.0 mm². At the Mg *K*-edge (1303.0 eV as edge energy), the resolution of the photon energy was less than 0.5 eV. As described in the above section, low-energy secondary electrons constitute a significant fraction of the spectra in this mode. Because the penetration range is less than 38 nm into the bulk, the XANES spectra reflect the structure of the samples in “near-surface region”.^{24,25} The photon energy was calibrated at the Al *K*-edge (1559 eV) using an aluminum metal-foil. Fourier transformed EXAFS (k^3 -weighted) was obtained within the range $\Delta k = 2.0$ – 7.5 Å^{−1} without any shift correction by the method described elsewhere.³¹

It is well-known that MgO and doped MgO chemisorb water vapor and carbon dioxide. To avoid the exposure of the samples to air as possible, the sample setting in all of the measurements was as carried out under the flowing N₂ or He atmosphere by using a conventional dry glovebox or packing made of polypropylene film. The preparation of the sample for each measurement described below was carried out in this procedure. In this setting procedure, most of chemisorption can be avoided and structural change of MgO by the chemisorption is less seen in the XANES spectra.²⁶ To make sure, contamination with CO₂ in air was appreciated by means of C 1s peak of XPS spectra.

For all the samples, C 1s peak with vary small intensity was seen, but it disappeared by the Xe sputtering within 10 s.

XRD spectra were recorded using a Rigaku Geiger-Flex 2102 X-ray diffractometer using Cu K α radiation filtered with a Ni foil. Each sample (1.5 g) was mixed mechanically with NaCl (0.5 g) as a reference sample and used for XRD measurement. The diffraction intensity of the samples was normalized to that of a standard sample. In the diffraction patterns shown in this paper, the diffraction peaks of the reference were removed.

The scanning electron microscopy (SEM) images were taken on a Hitachi S-800 FEG microscope with an accelerating voltage of 20 kV using conventional sample preparation and imaging techniques. Before the microscopic analysis, Pt–Pd coating (ca. 10 nm of thickness) was carried out for each sample by metal evaporation method using a plasma-induced Pd–Pt filament.

XPS spectra were measured using a Φ model 5500 spectrometer with Mg K α (15 kV to 400 W) emission for the X-ray source. Each sample was mounted on the indium foil and placed in a sample holder. Binding energy was calibrated using the C 1s photoelectron peak (284.6 eV). Near-surface composition of Li and Mg was evaluated from the integrated areas of Li 1s and Mg 2p regions quantified using the normal factors. Variation of the concentration with depth was investigated by Xe ion etching. The sputtering rate was approximately 3.0 nm min^{−1}, as estimated previously via a CuO/Cu sputtering experiment.

UV–vis spectra were obtained in a diffuse reflectance mode by using Perkin-Elmer Lambda-19 spectrometer at room temperature. The measured samples were packed with the polyethylene film under N₂ atmosphere.

Specific surface area of each sample was estimated by B.E.T. method by using N₂ physisorption at 77 K. The sample after the reaction was collected under He atmosphere and put on the adsorption cell.

OCM Reaction. The OCM reaction over Li–MgO catalysts with various Li concentrations was carried out using a fixed-bed flow reactor with an on-line gas chromatograph. The catalyst sample (0.5 g) was set in a ceramic tube reactor. As pretreatment, each catalyst sample was treated at 873 K for 1 h in an O₂(2.3%)/He(97.7%) stream before the OCM reaction. The reactor was then cooled and kept at 573 K for 10 min. After pretreatment, a gas mixture containing CH₄(9.4%)/O₂(2.3%)/He(88.3%) was fed to the reactor for the OCM reaction. The flow rate of the gases was controlled by means of mass-flow controllers (KOFLOC, Model-3650). The total flow-rate was 66.5 cm³ min^{−1} in both the pretreatment and reaction. In the case of rising temperature reaction (as a non-steady-state reaction), the reaction temperature was raised from 573 to 1173 K at a rate of 5 K min^{−1} and then kept at 1173 K for 60 min. In the steady-state reaction case, this was carried out successively at 1073 K with the same composition and flow rate of the reaction gas as for the non-steady-state case. For each reaction mode, the product gas was analyzed periodically by means of two gas chromatographs with columns packed with Porapak-Q (for CH₄, CO₂, C₂H₄, C₂H₆, HCHO, and CH₃OH) and Unibeads-C (for CO and O₂). After the reaction, the catalyst sample was treated with He for more than 5 min, and cooled to room temperature overnight in a He atmosphere. The catalyst sample after the reaction was collected and was subjected to XRD and XANES measurement.

Results and Discussion

1. XRD. Figure 1 shows the XRD patterns of Li–MgO with various levels of Li-doping. For all samples, diffraction peaks due to rock-salt MgO are clearly seen. The relative intensity of

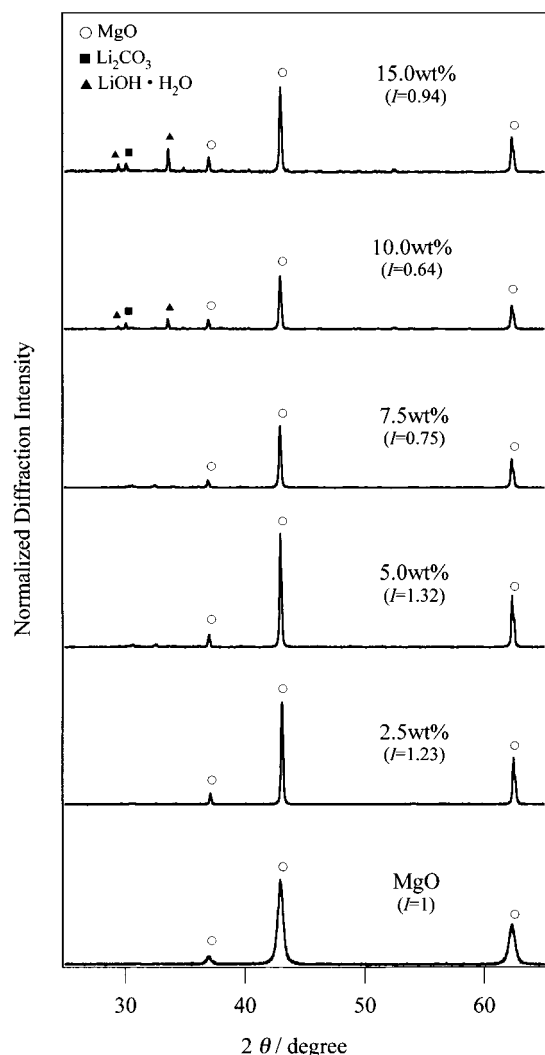


Figure 1. X-ray diffraction patterns of Li-doped MgO. (*I* shows the relative intensity of MgO(200) diffraction.)

the MgO(200) diffraction in each sample is also shown in the figure. For low Li content, the intensity of the diffraction peaks due to the MgO phase increases with an increase in the Li content up to 5.0 wt %, indicating that Li-doping enhances the crystallization of MgO. This feature supports the many reports about the affects of the addition of small amount of Li ions to MgO. For higher levels of Li-doping, more than 7.5 wt %, the intensity of the MgO peaks is smaller than that of nondoped MgO. This suggests that the increased amounts of Li ion has the effect of inhibiting the formation of a long-range ordered MgO structure. In addition, $\text{LiOH}\cdot\text{H}_2\text{O}$ and Li_2CO_3 phases can be detected in Li-rich samples at above 7.5 wt %. Presumably doped Li ions diffuse in/on MgO and for more than 10 wt %, excess Li ions form separated lithium hydroxide and carbonate phases.

2. Mg K-edge XAFS. Figure 2 shows the Mg K-edge XANES spectra of reference Mg compounds (a) and Li-MgO samples (b). For Li-MgO samples of above 5.0 wt % Li, each XANES spectrum is closely similar to that of MgO. This indicates that the rock-salt MgO structure is dominant in the near-surface region. It is noted that the spectrum in 2.5 wt % Li-MgO is different from those of the higher level Li-doped samples and MgO. This indicates definitively that Li-doping at a low level brings about a structural change in the near-surface region only. This phenomenon was also observed for Mn-doped

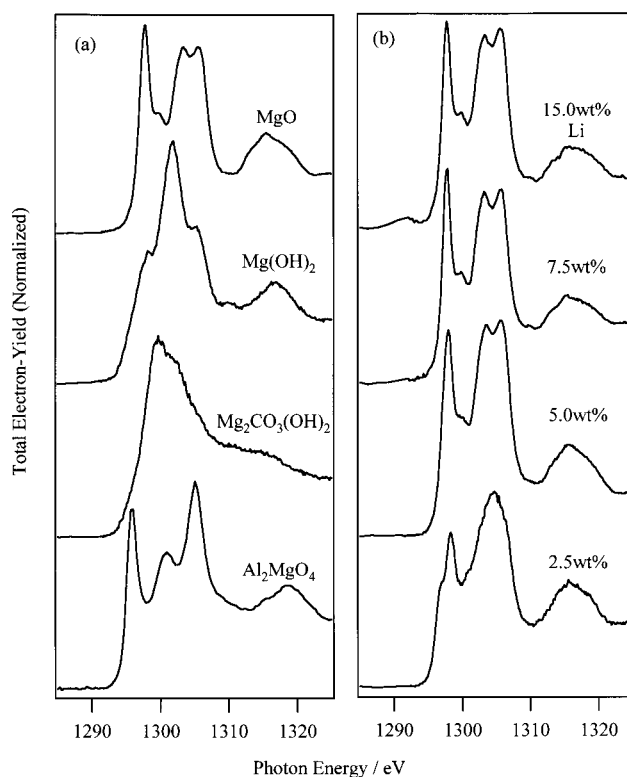


Figure 2. Mg K-edge XANES of reference compounds (a) and Li-doped MgO (b).

MgO, as described in the previous report.²⁸ From the XRD results above, the 2.5 wt % Li-MgO contains a bulk MgO phase with high crystallinity. Therefore, structural change should occur in the near-surface region, and the coexistence of rock-salt structure due to MgO and other structural components can be realized.

The edge energy of XANES can be obtained by using the first derivative of XANES. The energy at maximum point in the derivative spectrum reflects the threshold position of XANES directly. The derivatives of XANES spectra are shown in Figure 3. The spectrum of Al_2MgO_4 , which has a spinel structure where all Mg cations occupy a tetrahedral site, exhibits an edge peak at 1294.5 eV. For MgO with rock-salt structure, the edge energy is determined as 1296.9 eV. The energy values of other samples with distorted Mg-O₆ octahedron, $\text{Mg}(\text{OH})_2$ (CdI-type structure) and $\text{Mg}_2\text{CO}_3(\text{OH})_2$ (mixture of several types of distorted octahedron) are higher than that of MgO. The order of edge energy, (tetrahedron (T_d)) < (octahedron (O_h)) < (distorted octahedron), is appropriate to not only Mg but also many target atoms. Since XANES is associated with the excitation of a core electron to bound and quasi-bound states, the spectral feature of XANES must be dominated therefore by local structure around absorption atoms.³² For typical metal compounds, it has been reported that the position of an edge peak can be found at the lower energy side when the cation is in a lower coordination with the same valence.³²⁻³⁵ According to Mg K-edge XANES, the absorption is due to the electron transition from 1s to 3p orbital mainly in the near-edge. The energy level of Mg 3p in Mg-O₄ tetrahedron (T_d) is lower than that of Mg-O₆ octahedron (O_h). The level of distorted octahedron becomes higher than that of O_h octahedron because of broadening and/or splitting of 3p σ^* state. Thus, the energy position reflects the coordination number and/or ionicity (electronic state) directly, and the similarity of the spectral features means directly the existence of similar structure.

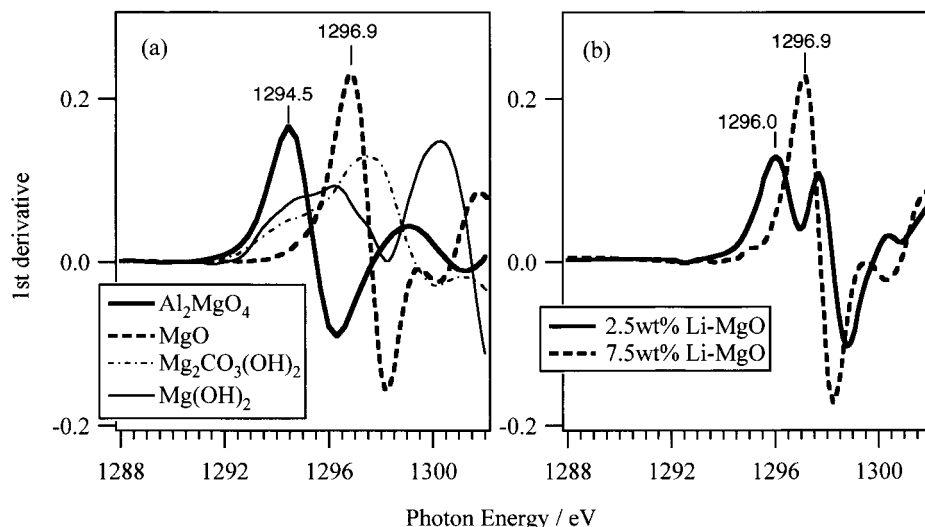


Figure 3. First derivatives of XANES spectra for evaluation of edge energy: (a) reference Mg compounds; (b) 2.5 and 7.5 wt % Li-MgO.

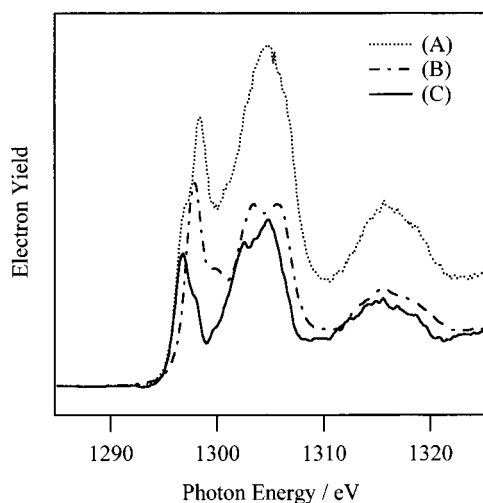


Figure 4. XANES spectrum of Li(2.5wt%)-MgO and difference spectrum obtained by subtracting that of MgO (55%): (A) original XANES spectrum of Li-MgO; (B) XANES spectrum of MgO with 55% intensity; (C) difference spectrum (A - B).

In the case of 7.5 wt % Li-MgO, the edge energy of XANES is the same as that of MgO, indicating that rock-salt structure is dominant. For XANES spectrum of 2.5 wt % Li-MgO, the edge energy positioned at 1296.0 eV should be noted. The energy of 2.5 wt % Li-MgO is a little lower than that of MgO (1296.9 eV) but is higher than that of Al_2MgO_4 (1294.5 eV). If the local structure consists of hepta-coordinated ones only, the edge energy should be higher than that of MgO with O_h symmetry. Therefore, it can be suggested that the major structure is coordinately unsaturated Mg cations such as tetra- and/or pentacoordinated species. On the assumption that the spectrum contains components due to rock-salt MgO and another unidentified species, we can suggest that the component due to this latter species can be estimated by subtraction of MgO-based spectral components from the real spectrum of 2.5 wt % Li-MgO system. For example, resultant spectrum is depicted as a solid curve (C) in Figure 4, which was obtained by subtraction of a 55%-weighted MgO spectrum. Differently weighted MgO contributions gave obscure or unlikely spectra. An intriguing point is that the features of the spectrum (C) are very similar to those of MgO although the energy position is 1.0 eV lower than that of MgO. In addition, the features of spectrum (C) were quite different from those of $\text{Mg}(\text{OH})_2$, $\text{Mg}_2\text{CO}_3(\text{OH})_2$, and Al_2MgO_4 shown in Figure 2a. It is reasonable to suppose that low coordinated Mg ions with MgO-like local structure coexist with rock-salt MgO structure. A Mg atom in the unidentified species is presumably located at a specific site like an edge or a corner, which can be formed adjacent to oxygen vacancies. The formation of the vacancy defects and the penetration of Li ions can enhance the base strength which stabilizes the lowest levels of unoccupied states resulting in the shift of the XANES spectrum of the unknown species to a lower energy.

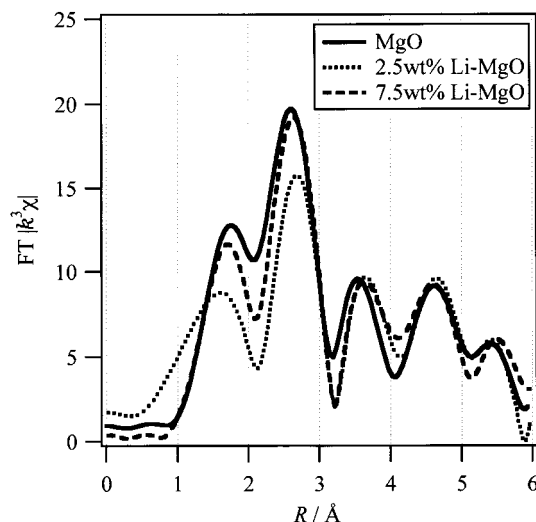


Figure 5. Fourier-transformed k^3 -EXAFS of MgO and Li-MgO.

To clarify the formation of defects, the analysis of Fourier transformation of k^3 -weighted EXAFS on the samples was applied. The results of FT-EXAFS are shown in Figure 5. The peak at around 1.6–1.8 and 2.6–2.7 Å should be due to the multiple scattering of first O (Mg–O bond) and second Mg (Mg–(O)–Mg) shells, respectively. The intensity of each peak relates to the mean coordination number.³⁶ The differences of the energy value in the first peak between these samples can be noted. For 7.5 wt % Li-MgO, the peak intensity of the first shell is a little smaller than that of MgO, indicating the slightly lower coordination number of Mg–O bond. For 2.5 wt % Li-MgO, the first and second peaks are less intense than MgO and 7.5 wt % Li-MgO. This possesses the existence of lower-coordinated Mg ions in near-surface than MgO. In addition, the peaks due to higher shells at above 3.5 Å are almost similarly

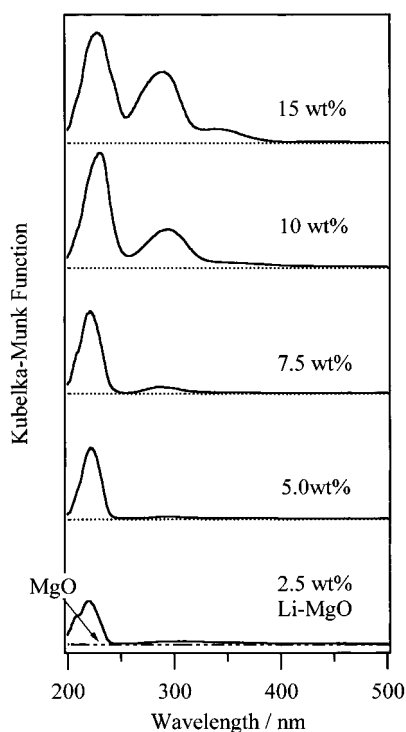


Figure 6. Diffuse reflectance UV-vis spectra of Li-MgO.

between three samples. This result strongly supports the formation of defects on 2.5 wt % Li-MgO.

It is well-known that F-center is formed onto MgO when defect site is stabilized in the bulk phase, and the center can absorb the UV-vis light. Thus the UV-vis spectroscopy was employed to clarify the formation of defects by Li-doping on MgO. Because the UV-vis spectra were measured in a diffuse reflectance mode, the structural information contains not only in the surface region but also in the bulk phase. The spectra are shown in Figure 6. Nondoped MgO shows no absorption. The absorption at 360 nm, which can be seen as hydroxycarbonate species in atmosphere exposed magnesia,³⁷ is invisible in all of the samples. By promotion of Li ions, the absorption bands are detectable. For 2.5–5.0 wt % Li-MgO, the band centered at 240 nm can be seen. This absorption band can be assigned the CT band in $\text{Mg}^{2+}-\text{O}^{2-}$ with lower (about 4) coordinated Mg

ions.^{38,39} For above 7.5 wt % of Li-MgO, a new absorption band at around 280 nm is visible and the ratio of this peak increased with an increase in Li-doping amount. This band can also be due to the defects where lower (about 3) coordinated Mg ions are formed.³⁸ These absorption bands were not observed on MgO single crystal. These results by UV-vis spectroscopy also support the formation of defect sites by Li-doping, and the state of defect sites is different between 2.5 wt % and more than 7.5 wt % of Li. As described in this section, it can be concluded that Li-doping onto MgO brings about the formation of defect species.

3. XPS. To obtain detailed information about structural differences between 2.5 wt % and 7.5–15.0 wt % Li-MgO, we characterized the states of surface Li and Mg ions by means of XPS. We also measured a depth profile of the Li ion by using Xe-sputtering. Figure 7 shows the Li 1s, Mg 2s, and O 1s photoelectron peaks of Li-MgO samples before sputtering. For all samples, the Mg 2s intense peaks resemble each other, indicating that the state of Mg-O bonds is independent of the Li-doping. The energy of those Mg 2s peaks is the same as the binding energy of rock salt MgO. These peaks show no change following by Xe sputtering for 10 min, as shown in Figures 8. On the other hand, the doped Li content makes a difference to the O 1s peaks. For each sample, a primary peak at 533 eV and a shoulder around 531 eV can be seen in Figure 7. These two peaks in higher and lower energy sides are possibly due to rock salt MgO and lithium carbonate species, respectively. The shoulder peak at 531 eV disappeared on sputtering (Figure 8), indicating that carbonate species only exists in the surface of Li-MgO. For 7.5 and 15.0 wt % Li-MgO, another peak at ca. 535 eV is also seen. This peak in the 15.0 wt % Li-MgO case is more intense than that in the 7.5 wt % sample and scarcely seen in the 2.5 wt % Li-MgO system. This peak should be due to oxygen anions coordinated with Li ions. Thus, it can be suggested that the higher amounts of Li-doping above 7.5 wt % bring about formation of Li-O bonds in the surface region, and when rich in Li ions gives an increase in Li-O sites in the surface. For Xe-sputtered samples, the photoelectron spectra are quite different from those nonsputtered. In the case of the 7.5 and 15.0 wt % Li-doped samples, a primary peak due to rock salt MgO and a shoulder due to Li-induced species are seen. For 2.5 wt % Li-MgO, a peak due to the MgO phase is also seen at 533 eV; however, the shoulder peak at around 535 eV

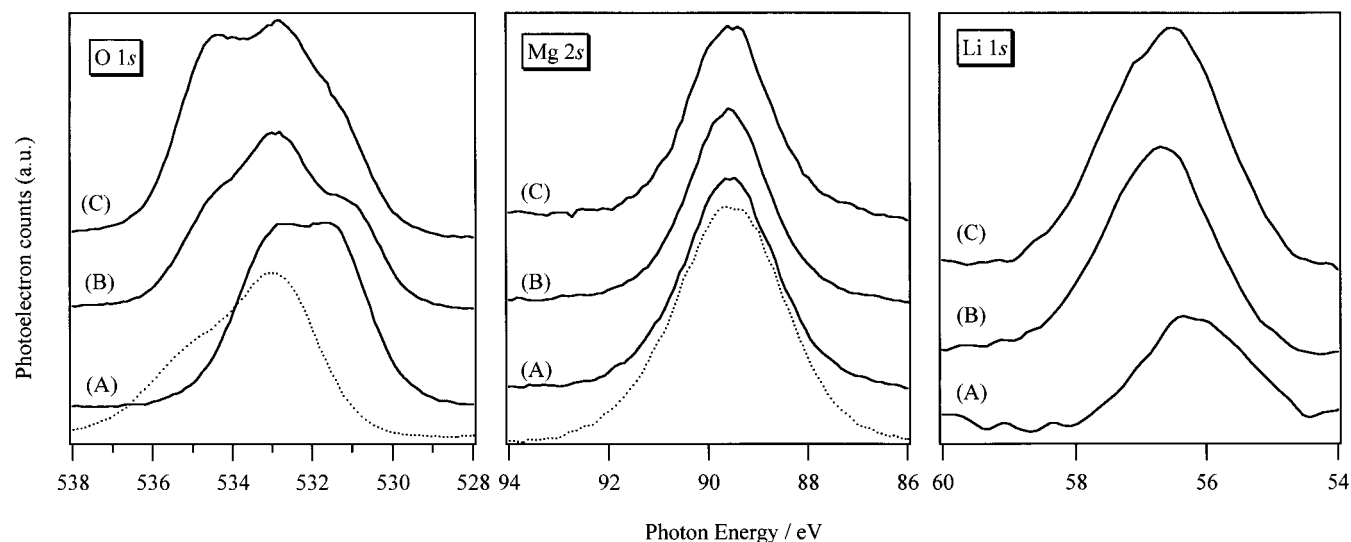


Figure 7. XPS spectra of Li-doped MgO (before sputtering): (A) 2.5 wt %, (B) 7.5 wt %, and (C) 15.0 wt % Li-doping. Dotted lines are the spectra of non-doped MgO.

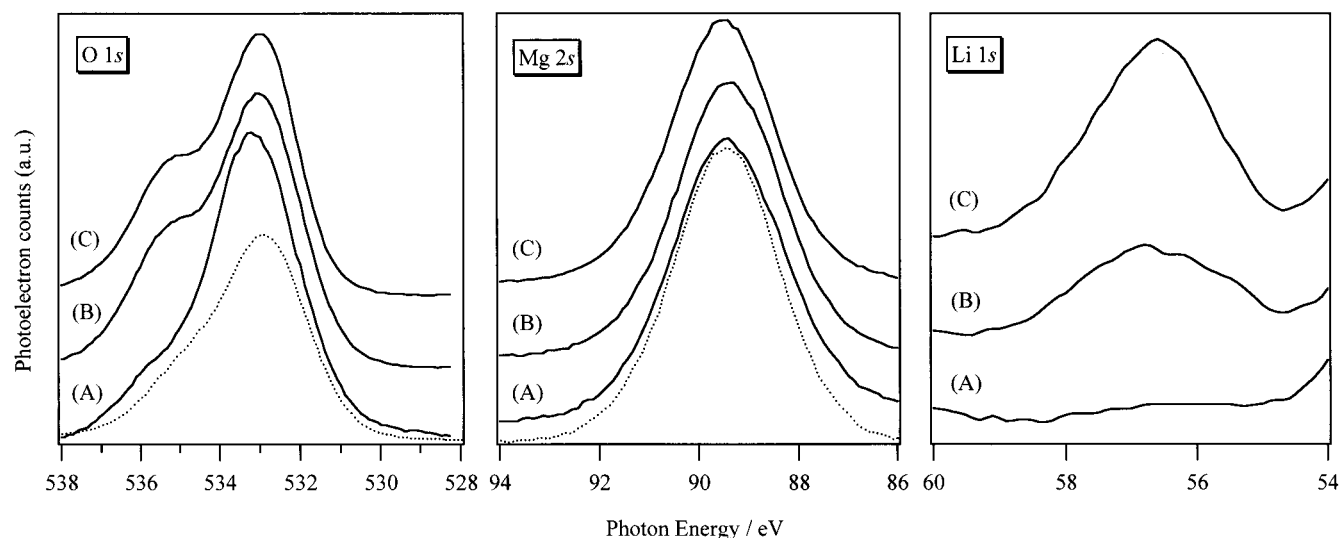


Figure 8. XPS spectra of Li-doped MgO after Xe-sputtering for 10 min: (A) 2.5 wt %, (B) 7.5 wt %, and (C) 15.0 wt % Li-doping. Dotted lines are the spectra of non-doped MgO.

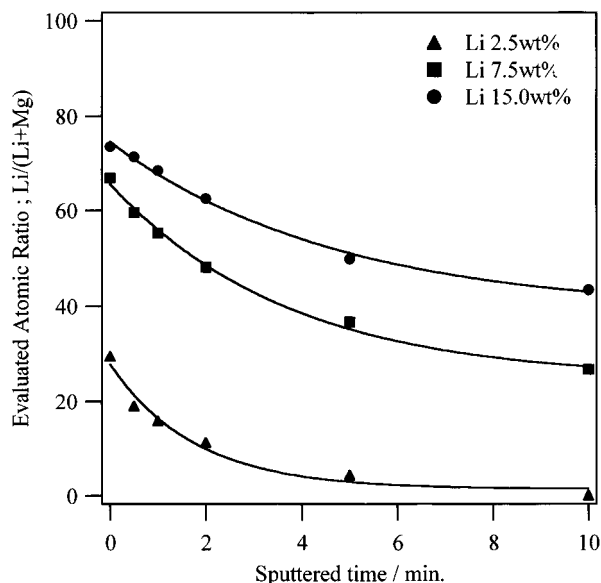


Figure 9. Depth profile of Li concentration in Li-MgO.

is absent. It is likely that doped Li ions have a tendency to localize in the surface. In the case of the Li 1s photoelectron peaks, the energy position for 7.5 wt % Li-MgO case before sputtering is almost similar to that of the 15.0 wt % sample. However, the band position for 2.5 wt % Li-MgO is lower than that of high Li-content samples, indicating that Li-O bonds are formed in the surface. After Xe-sputtering, each Li 1s photoelectron count becomes small. In particular, the Li 1s peak of the 2.5 wt % Li-MgO is almost lost. This result supports the above suggestion about the localization of Li ions in the near-surface region. In fact, aggregated Li ions in the surface of MgO can be stabilized as ionic clusters such as Li_3^{2+} .⁴⁰ Therefore, the distribution of Li ion in/on MgO needs to be clarified.

We estimated the Li concentration by means of an XPS depth profile. The spectra of Li 1s and Mg 2s regions were recorded through a stepwise sputtering with Xe ions. The results of the depth profile for the Li-MgO samples are shown in Figure 9. In all samples, relative Li concentration ($=\text{Li}/(\text{Li}+\text{Mg})$) decreases with an increase in sputtering time. Therefore, it can be concluded that Li ions tend to localize in the near-surface of MgO. For 2.5 wt % Li-MgO containing 13.0 mol % of Li, the

surface Li concentration is estimated as about 30 mol %. However, subsurface Li can hardly be seen after sputtering for 10 min. This shows that doped Li ions at a low content (2.5 wt %) exist only in the near-surface. On the other hand, Li ions clearly exist in the subsurface for the 7.5 and 15.0 wt % Li-MgO. It can be concluded that, when abundant, Li ions penetrate the bulk phase and bring about a decrease in MgO crystallinity, as shown in the XRD data. Noted difference of Li-MgO between high (7.5–15.0 wt %) and low (2.5 wt %) Li contents is whether the Li ions exist in the bulk phase or not.

Judging the results described above, doped Li ions at a low level (2.5 wt %) may promote the formation of oxygen defects localized in the near-surface. From the XPS results, in summary, Li ions do not exist diffused in the bulk but localize on the MgO surface. However, only the surface oxygen sites due to rock-salt MgO and carbonate species can be seen. If the structural change in the near-surface is due to the formation of other phases, which are different from MgO, new photoelectron peaks should be seen at O 1s and/or Mg 2s region. However, no new peaks are obtained. It may be possible that surface Li ions affect a change of the surface MgO structure but do not determine the state of both Mg and O ions in the surface. Therefore, it is reasonable to assume that Li ions in the low content sample contribute to the formation of defect sites in the MgO surface. On this assumption, it is concluded that Li ions are dispersed on the MgO surface and are found as Li^+-O^- sites. At higher Li contents of 7.5–15.0 wt %, Li ions exist not only in the near-surface but also in the bulk phase. However, defect sites in the near-surface are scarcely formed at the higher Li contents. According to the surface characterization, Lunsford et al. reported¹¹ that intensity of an ESR signal due to surface Li^+-O^- sites increases with an increase in Li-doping below 15.0 wt %, but many workers including them pointed out that bulk defect sites are important for OCM recently.^{1,11,41} It can be suggested that the Li^+-O^- sites diffuse into MgO because of the existence of Li ions in the bulk phase of MgO. In addition, surface Li ions affect the structural change of rock-salt MgO, as discussed from the XANES results in the above section. From the XRD results, separated $\text{LiOH}\cdot\text{H}_2\text{O}$ phase could be observed, supporting the tendency of Li-aggregation. It can be concluded that bulk Li ions affect the formation of defect species onto MgO, and surface Li ions tend to form the separate phase which hardly affect the surface MgO structure.

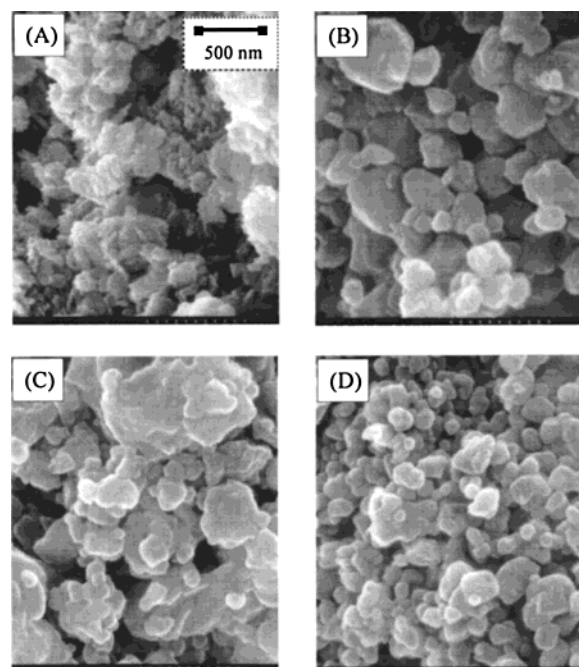


Figure 10. SEM image of Li-doped MgO: (A) MgO, (B) 2.5 wt % Li, (C) 7.5 wt % Li, and (D) 15.0 wt % Li-doping.

4. SEM. To obtain direct information on MgO crystallinity, scanning electron microscopy (SEM) is employed. The SEM images are shown in Figure 10. To compare the MgO crystallinity in a similar preparation condition, MgO was prepared as a reference by impregnation of calcined MgO powder with pH-controlled ($\text{pH} = 9$ using NH_4OH) aqueous solution without Li ions, followed by drying and calcination at 873 K. For these MgO samples, the many small particles with low crystallinity can be seen. In the case of 2.5 wt % Li-MgO, large crystalline particles of MgO are clearly seen, indicating that an enhancement of crystallization is brought about by the low amount of Li-doping. This supports the result of XRD analysis. However, in the image of 7.5 wt % Li-MgO, the particles are much less distinctive than those of a 2.5 wt % Li sample. It also supports the decrease in MgO crystallinity obtained by XRD. However, the surface Mg ion has a MgO-like local structure as clarified by XANES, and Li ions exist not only in the surface but also in the bulk phase of MgO as shown by XPS. It is proposed that the dispersed Li ions exist in not only the surface but also the bulk phase. Thus the Li ions scarcely affect a structural change of surface MgO, but each MgO particle appears to be overlaid with a lithium hydroxide or carbonate layer. In fact, higher Li-doped sample shows those Li phases as investigated by XRD. In the case of 15.0 wt % Li-MgO, the smaller crystalline particles are clearly visible than 2.5 or 7.5 wt % Li samples. The definite phases which may be assigned to lithium hydroxide or carbonate can be seen in this sample, and therefore, the visible particles in the SEM image can be assigned as both MgO- and Li-induced phases. It is concluded that the Li-induced species scarcely affects a structural change in the surface MgO phase, and the local structure around Mg ions is retained.

5. OCM Reaction. As described above, Li-doped MgO is well-known as an OCM catalyst. We also investigated the catalytic activity of Li-MgO for the methane coupling reaction, and characterization of the catalyst samples after the reaction was carried out. The composition ratio of the reaction gas is about $\text{CH}_4/\text{O}_2 = 4$. Figure 11 shows the catalytic activity of Li-MgO samples as a function of the reaction temperature increased at a rate of 5 K min^{-1} . For nondoped MgO, conversion

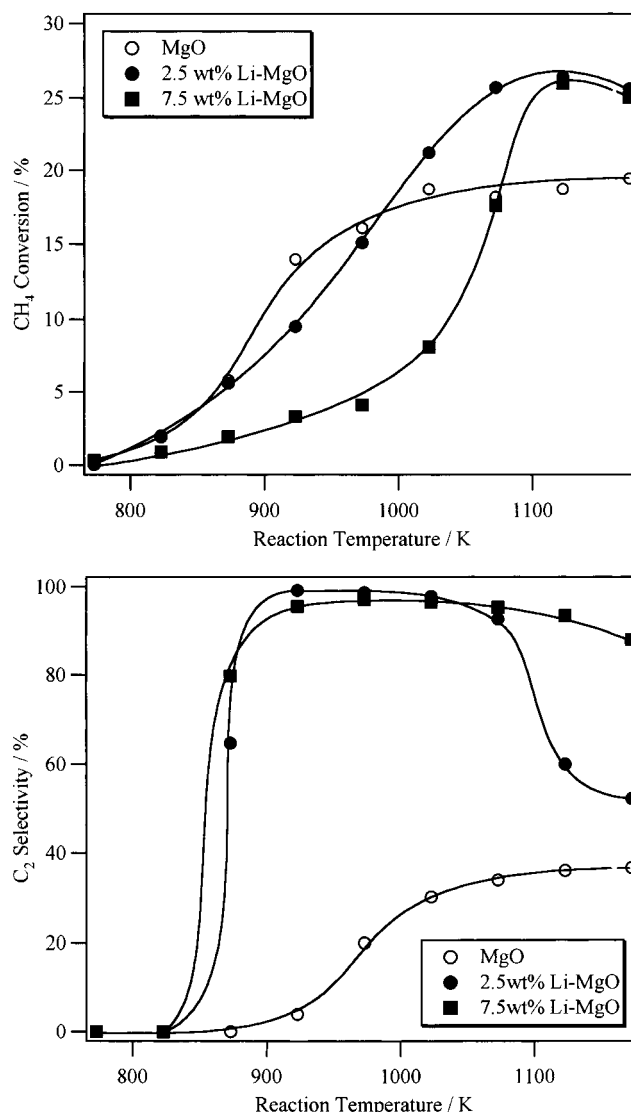


Figure 11. OCM reactivity (CH_4 conversion and C_2 selectivity) over Li-MgO catalysts under elevating reaction temperature (5 K min^{-1}).

of methane reaches about 20% at 1173 K, but C_2 selectivity is less than 40% even at high reaction temperature. However, deactivation is scarcely seen. Thus, MgO catalyst has a stable species with low activity for OCM. Li-doped MgO shows a higher conversion than MgO at relatively high temperature around 1100 K, and the C_2 selectivity is more than 90% at 923–1073 K. These results indicate the generation of active species for OCM following Li doping. However, the material balance of carbon for reactants and products was inconsistent because the reactant carbon in methane is partly consumed in forming a carbonate species or phase in/on the catalyst. This indicates that the reaction is non-steady state. After reaction at 1173 K for 1 h, the number of carbons in the product gas became equivalent to that in the reactant stream. To compare the reactivity under steady-state reaction conditions, a successive reaction at 873 and 1073 K for 240 min was carried out. The result is shown in Tables 1 and 2. For 2.5 wt % Li-MgO, C_2 selectivity is less than 18% in the reaction at 873 K, and the selectivity reaches 70% at 1173 K. On the other hand, high C_2 selectivity (more than 84%) is obtained for 7.5 wt % Li-MgO in the initial step of the reaction at 873 and 1173 K. Thus, high temperature needs to bring about the C_2 selectivity for 2.5 wt % Li-MgO. Figure 12 shows the time course of the reaction at 1173 K. For Li-doped MgO, rapid deactivation for converting

TABLE 1: OCM Reactivity over MgO and Li–MgO at 873 K

catalyst	reaction time (min)	methane conv. (%)	selectivity (%)			
			CO ₂	CO	C ₂ ^a	others ^b
MgO	5	3.0	97	3	0	
	30	3.9	97	3	0	trace
	60	4.4	96	4	0	trace
	240	4.7	97	3	0	trace
2.5 wt % Li–MgO	5	5.2	85	3	12	trace
	30	5.7	85	3	12	trace
	60	6.4	86	3	11	trace
	240	6.6	80	3	18	trace
7.5 wt % Li–MgO	5	5.0	0	6	94	trace
	30	4.4	5	10	85	trace
	60	3.6	8	8	84	trace
	240	2.9	58	0	42	trace

^a C₂H₄ + C₂H₆. ^b Containing HCHO and HCOOH.**TABLE 2: OCM Reactivity over MgO and Li–MgO at 1173 K**

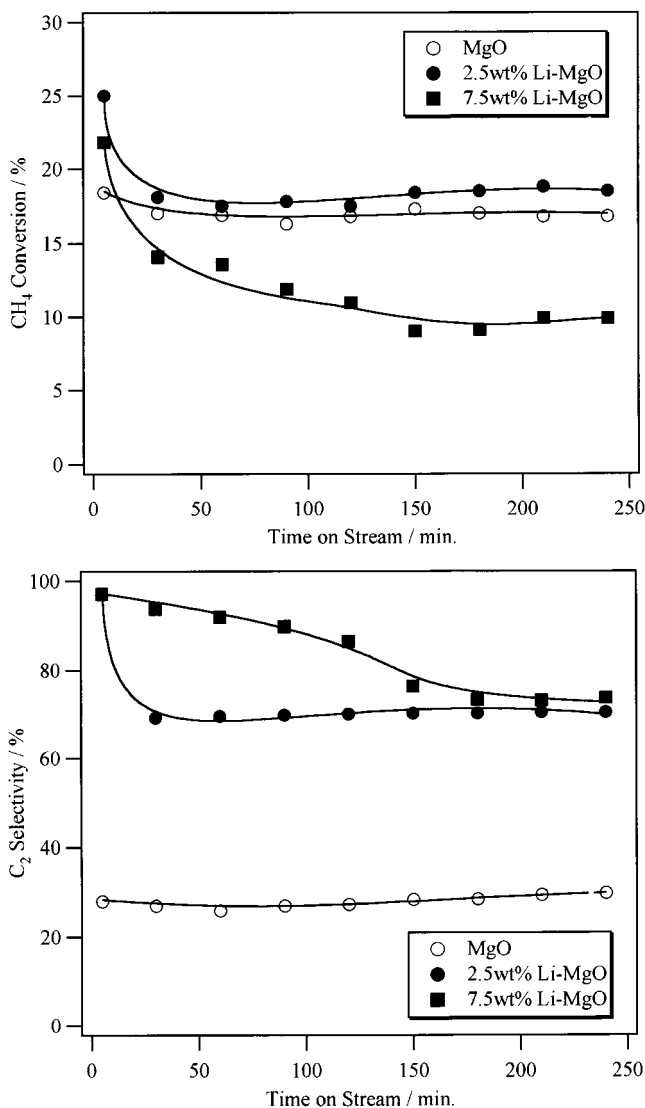
catalyst	reaction time (min)	methane conv. (%)	selectivity %			
			CO ₂	CO	C ₂ ^a	others ^b
MgO	5	18.4	70	2	28	trace
	30	17.0	72	1	27	trace
	60	16.9	73	1	26	trace
	240	16.8	69	1	30	trace
2.5 wt % Li–MgO	5	25.0	3	0	97	trace
	30	18.1	31	0	69	trace
	60	17.5	30	0	70	trace
	240	18.5	30	0	70	trace
7.5 wt % Li–MgO	5	21.8	3	0	97	trace
	30	14.1	6	0	94	trace
	60	13.6	8	0	92	trace
	240	9.9	26	0	74	trace

^a C₂H₄ + C₂H₆. ^b Containing HCHO and HCOOH.

methane can be seen during the initial reaction time. After achieving steady-state conditions, the methane conversion on 7.5 wt % Li–MgO is lower than that on MgO and 2.5 wt % Li–MgO before the reaction. This indicates that only a high amount (7.5 wt %) of Li-doping gives a low activity for converting methane. The C₂ selectivity on Li–MgO catalysts is higher than that on fresh MgO. The decrease in the production of C₂ compounds over Li–MgO may be due to the formation of carbonate and/or hydroxide species.^{42,43} In the steady state, the C₂ selectivity reaches almost 75% on both 2.5 and 7.5 wt % Li–MgO samples. The trend in of these OCM results partially support the conclusion on the catalytic activity of Li–MgO catalysts reported by many workers.

The results of specific surface area of MgO and Li–MgO before/after the OCM reaction at 1073 K for 240 min are shown in Table 3. Before the reaction, the specific surface areas of MgO and Li–MgO (both 2.5 and 7.5 wt % Li) were 69 and 2 m² g^{−1}, respectively. It indicates that the surface area reduces excessively by Li-doping, supporting the discussion of the characterization by means of XRD and SEM, as described in the above section. After the reaction, the value of surface area of MgO and 2.5 wt % Li–MgO reduced drastically, and became about one-fourth. On the other hand, 7.5 wt % Li–MgO shows less change after reaction. The stability of bulk structure may different between 7.5 wt % and 2.5 wt % Li–MgO. For these samples, higher OCM reactivity is shown despite the smaller surface area than that of MgO. However, the relation between the specific surface area and the OCM reactivity could not obtained clearly.

We characterized the surface and bulk species of Li–MgO catalysts after the OCM reaction at 1173 K for 1 h. The XRD patterns of the samples after reaction are shown in Figure 13. For Li–MgO samples, a lithium–carbonate phase can be

**Figure 12.** OCM reactivity (CH₄ conversion and C₂ selectivity) of Li–MgO catalysts under steady-state reaction at 1073 K.**TABLE 3: Specific Surface Area of Li–MgO before and after the Reaction at 1023 K for 3 h**

catalyst	surface area (m ² g ^{−1})	
	before reaction	after reaction
MgO	69	16
2.5 wt % Li–MgO	2	0.5
7.5 wt % Li–MgO	2	2

observed clearly. The carbonate phase is formed during the OCM reaction because it is absent before the reaction. The MgO phase is visible only, and another magnesium-containing phase (such as Mg(OH)₂, MgCO₃, or Mg₂CO₃(OH)₂) is not observed. The order of MgO crystallinity is shown: (2.5 wt % Li–MgO) > (7.5 wt % Li–MgO) > (nondoped MgO). The order is not as same as that before the reaction. The results show that Li-doping may affects the inhibition of decrease of MgO crystallinity in the bulk phase. During the OCM reaction, it is likely that the formation phase-separated Li-phase (as lithium carbonate) occurs and MgO crystallinity is almost kept on in Li-doped MgO samples. According to the structure in near-surface region, XANES spectra of 2.5 wt % Li–MgO before and after reaction are shown in Figure 14. After the pretreatment at 1173 K (before the reaction), the spectrum (B) is almost as same as MgO. This indicates the diffusion of Li ions into the MgO, as similarly as

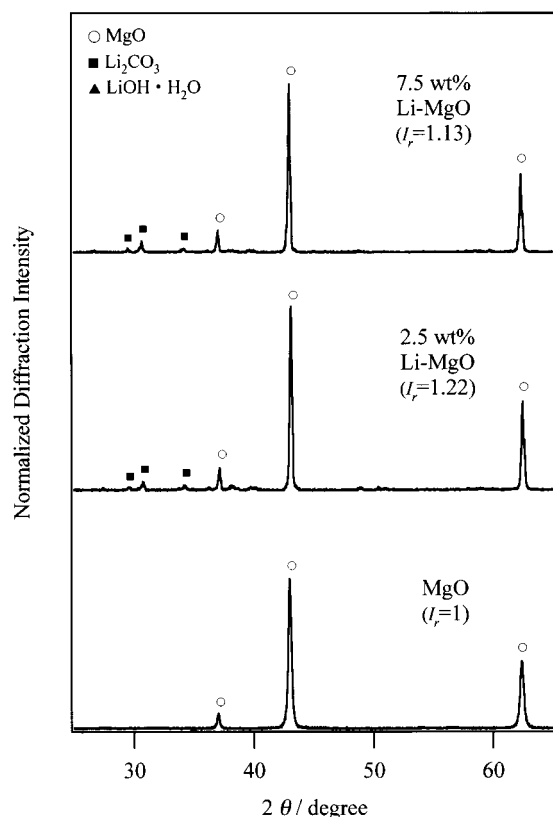


Figure 13. X-ray diffraction patterns of Li-doped MgO after OCM reaction at 1173 K for 1 h. (I_r shows the relative of MgO(200) diffraction.)

7.5 and 15.0 wt % Li–MgO. This result can be related to the OCM reactivity shown in Tables 1 and 2. In the case of the calcined sample at 873 K, Li ions are absent in the bulk phase and give a low C_2 selectivity. Thus, it is suggested that the formation of Li^+O^- sites in the bulk phase gives a high C_2 selectivity. After the OCM reaction at 1173 K, the spectrum (C), which possesses the re-formation of defect species, is obtained. Thus, it suggests that the phase separation to form lithium carbonate and MgO gives the formation of defects on MgO keeping on the relatively high crystallinity. The XANES spectra of the reacted Li–MgO samples with various Li amounts are shown in Figure 15. The spectra of the samples closely resemble each other. In addition, they are similar to that of 2.5 wt % Li–MgO (in Figure 2b) but different from MgO before the reaction. This result suggests the formation of a defective MgO structure in the near-surface region after the reaction. We tried to extract the other spectral component coexisting with MgO by using the same method as in the case of 2.5 wt % Li–MgO. The extracted spectrum of each sample after the reaction could be obtained appropriately (shown in Figure 15) by the subtraction of a weighted MgO spectrum with 45–55% intensity. The spectral features and the energy positions of these subtracted spectra also resemble those of fresh 2.5 wt % Li–MgO. In addition, other magnesium-derived species such as $Mg(OH)_2$ or $Mg_2CO_3(OH)_2$ (shown in Figure 3a) are not determined in the subtracted spectra. Thus, it can be proposed that the defect species is formed in the near-surface during the reaction. The formation of defect species in near-surface MgO is independent of the existence of Li ions, and these species play an active role in the catalysis of the OCM reaction. For Li–MgO samples, the defect species may be due to Li^+O^- centers. The Li^+O^- center should not be formed in MgO, but the defect structure in the near-surface is also formed during

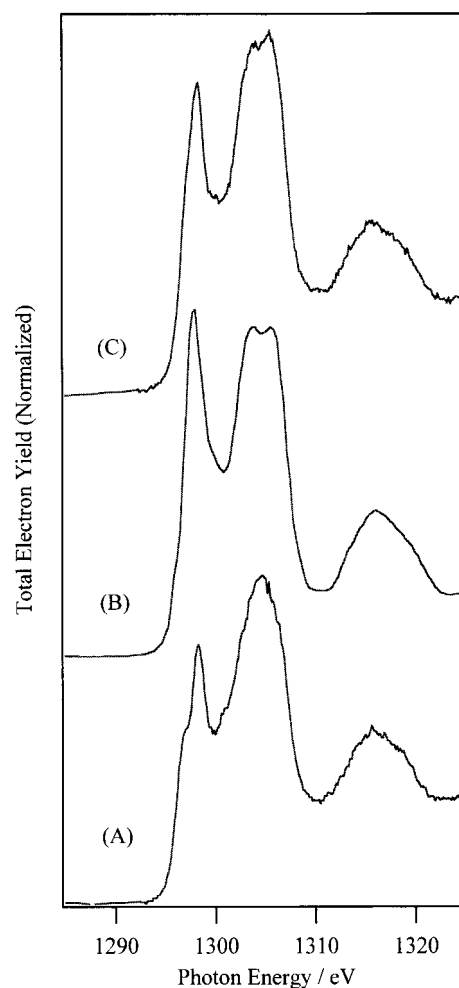


Figure 14. Mg K-edge XANES of 2.5 wt % Li–MgO: (A) calcined at 873 K; (B) after the pretreatment at 1173 K (before the reaction); (C) after the OCM reaction at 1173 K.

the OCM reaction. Figure 16 shows the FT-EXAFS of Li–MgO and nondoped MgO. Making a comparison between Figures 5 and 6, change of local structure can be seen during the OCM reaction. In particular, the intensity of first and second shells in MgO is lower than that of Li–MgO. This indicates that formed defect species during the reaction are different from those of Li–MgO. The R value of the first shell (Mg–O) in nondoped MgO after OCM reaction is smaller than that before reaction, and it may contain the $Mg(OH)_2$ -like local structure (shown in Figure 16). Thus it is possibly that local structure of defect species are slightly different between MgO and Li–MgO. The intensity of the first shell is ordered: (7.5 wt % Li–MgO) > (2.5 wt % Li–MgO) > (nondoped MgO). This order is also different from the bulk crystallinity of MgO, as shown in Figure 13. For these results, it is summarized that the amount of defect species in 7.5 wt % Li–MgO is smaller in the near-surface and larger in the bulk phase than those of 2.5 wt % Li–MgO. Taking the results into consideration, it is likely that the structural differences reflect the OCM reactivity.

From the results of the successive catalytic reaction, MgO has a stable defect species with lower activity than Li–MgO. We suggest that the formation of defect species in MgO brings about the generation of active species for OCM. With the existence of Li ions in MgO, the activity is enhanced. The Li^+O^- centers in both the bulk and near-surface region relate to the catalytically active species for OCM. It is considerable that

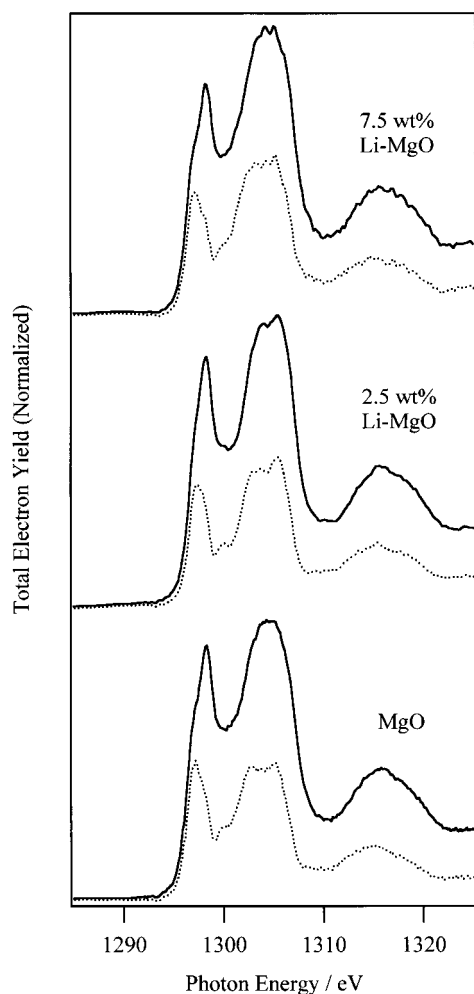


Figure 15. Mg K-edge XANES of Li-MgO after OCM reaction at 1173 K for 1 h. Dotted lines are the difference spectra obtained by subtracting the spectra of fresh MgO one with 55, 50, and 45% intensity for MgO, 2.5 wt % Li-MgO and 7.5 wt % Li-MgO, respectively. the difference of the OCM reactivity relates to the difference of bulk MgO crystallinity.

In the reaction at high temperature, the Li^+-O^- centers are in equilibrium with surface O^- centers via hole transport.^{3,10,11} The Li^+-O^- species not only surface but also bulk can induce the active species to form a methyl-radical in the reaction.¹¹ Therefore, not only surface but also bulk species can act as the catalytic species for OCM. For Li-MgO at a low Li content (2.5 wt %), CH_4 conversion and C_2 selectivity rapidly decrease in the initial stage of the reaction at 1173 K. Presumably Li ions partly form a separate lithium carbonate phase; however, defect species remain in the near-surface during the steady-state reaction. The defect species induced by the Li ions may act as the catalytic species for high CH_4 conversion. For 7.5 wt %, defect sites in the bulk phase with larger amount than that of 2.5 wt % Li-MgO. Thus, it is proposed that the defect sites in the bulk phase act as the active species for producing C_2 compounds with high selectivity. These can be summarized that near-surface defect sites reflect the CH_4 conversion and bulk defects give the C_2 selectivity. For Li-MgO, stable Li^+-O^- species exist as the defect species onto MgO with high crystallinity and can work the catalytic species for OCM.

Conclusion

In the preceding argument we have discussed the structural information of Li-MgO. The conclusion is summarized as follows:

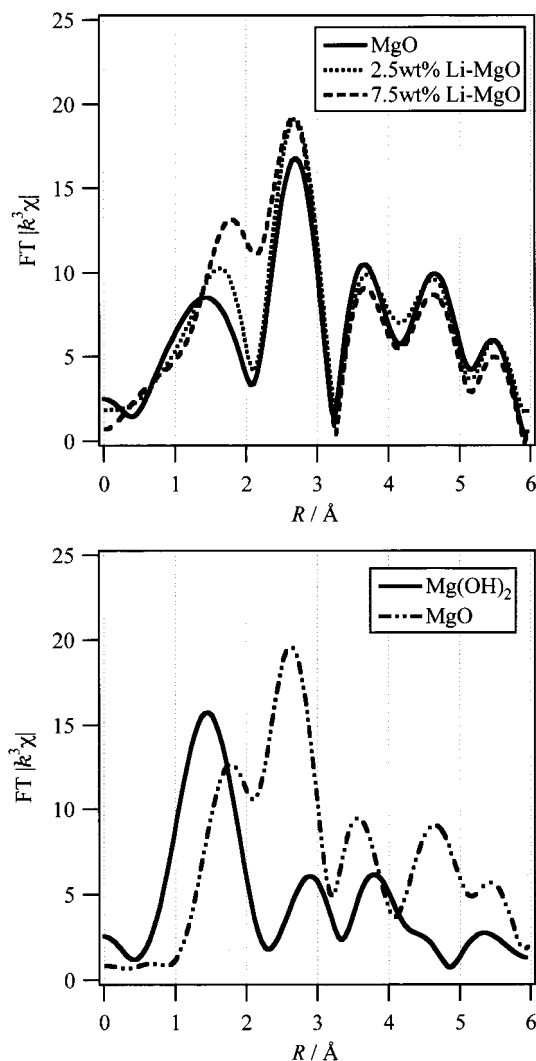


Figure 16. Fourier-transformed k^3 -EXAFS of MgO and Li-MgO after the OCM reaction at 1173 K (top) and reference compounds.

(1) For lower amount of Li-doping (at 2.5 wt %), Li ions doped on MgO tend to localize in near-surface region, giving the formation of defect species on MgO and affect the formation of bulk MgO with high crystallinity. For higher amount of Li-doping (at 7.5 wt %), Li ions exist not only in the near-surface but also in the bulk phase. In this case, the bulk crystallinity of MgO is reduced. Surface Li ions tend to form separated phase which hardly affect the surface MgO structure. The dispersion of Li ions, formed Li^+-O^- species, reflect the formation of defect species onto MgO.

(2) OCM reaction tends to bring about the formation of defect species in the near-surface of MgO. Li-doping on MgO affects the stabilization of bulk MgO crystallinity. For Li-MgO, the Li^+-O^- species (as the defect species onto MgO) in both the near-surface and the bulk phase can enhance the OCM reactivity. The dispersion of the Li^+-O^- species may reflect the OCM reactivity; a larger amount of near-surface defect sites affect the higher CH_4 conversion, and a larger amount of bulk defects tend to bring about the higher C_2 selectivity.

Acknowledgment. The X-ray absorption experiments at Mg K-edge were supported by the Joint Studies Program (Proposal No. 10-872, 1998 and others) of UVSOR in Institute for Molecular Science (IMS), Japan. We thank Dr. Eiji Shigemasa, and Mr. Osamu Matsudo (Institute for Molecular Science, Japan)

and Dr. Toyohiko Kinoshita (The University of Tokyo) for the supports of XANES measurements and helpful suggestions. Acknowledgment is given to Mr. N. Tanida for the measurement of BET surface area. We acknowledge the invaluable indication of the reviewer.

References and Notes

- (1) Lee, J. S.; Oyama, S. T. *Catal. Rev. Sci. Eng.* **1988**, *30* (2), 249.
- (2) Amenomiya, Y.; Birss, V. I.; Golezdzinowski, M.; Galuszkza, J.; Sanger, A. R. *Catal. Rev. Sci. Eng.* **1990**, *32* (3), 163.
- (3) Driscoll, D. J.; Martir, W.; Wang, J.-X.; Lunsford, J. H. *Adsorption and Catalysis on Oxide Surfaces*; Elsevier: Amsterdam, 1986; p 403.
- (4) Sokolovskii, V. D.; Mamedov, E. A. *Catal. Today* **1992**, *14*, 415.
- (5) Voskresenskaya, E. N.; Roguleva, V. G.; Anshits, A. G. *Catal. Rev. Sci. Eng.* **1995**, *37* (1), 101.
- (6) Guzzi, L.; van Santen, R. A.; Sarma, K. V. *Catal. Rev. Sci. Eng.* **1996**, *38* (2), 249.
- (7) Ito, T.; Lunsford, J. H. *Nature (London)* **1985**, *314*, 721.
- (8) Aika, K.; Lunsford, J. H. *J. Phys. Chem.* **1977**, *81*, 1391.
- (9) Maitra, A. M. *Appl. Catal. A* **1993**, *104*, 11.
- (10) Driscoll, D. J.; Lunsford, J. H. *J. Phys. Chem.* **1983**, *87*, 301.
- (11) Driscoll, D. J.; Martir, W.; Wang, J.-X.; Lunsford, J. H. *J. Am. Chem. Soc.* **1985**, *107*, 58.
- (12) Chen, Y.; Tohver, H. T.; Narayan, J.; Abraham, M. M. *Phys. Rev. B* **1977**, *96*, 5535.
- (13) Peng, X. D.; Stair, P. C. *J. Catal.* **1990**, *121*, 99.
- (14) Zhang, H.-S.; Wang, J.-X.; Lunsford, J. H. *J. Catal.* **1988**, *112*, 366.
- (15) Lin, C.-H.; Ito, T.; Wang, J.-X.; Lunsford, J. H. *J. Am. Chem. Soc.* **1987**, *109*, 4808.
- (16) Otsuka, K.; Said, A. A.; Jinno, K.; Komatsu, T. *Chem. Lett.* **1987**, *1*, 77.
- (17) Otsuka, K.; Jinno, K. *Inorg. Chim. Acta* **1986**, *121* (2), 237.
- (18) Otsuka, K.; Said, A. A. *Inorg. Chim. Acta* **1987**, *132* (1), 123.
- (19) Lin, C.-H.; Campbell, K. D.; Wang, J.-X.; Lunsford, J. H. *J. Phys. Chem.* **1986**, *90*, 534.
- (20) Louis, C.; Chang, T. L.; Kermarec, M.; LeVan, T.; Tatibouët, J. M.; Che, M. *Catal. Today* **1992**, *13*, 283.
- (21) Lunsford, J. H. In *Proceedings of the 10th International Congress on Catalysis*; Elsevier-Akadémi Kiadó: Budapest, 1992; p 103.
- (22) Balint, I.; Aika, K. *Stud. Surf. Sci. Catal.* **1994**, *81*, 177.
- (23) Balint, I.; Aika, K. *J. Chem. Soc., Faraday Trans.* **1995**, *91* (12), 1805.
- (24) Elam, W. T.; Kirkland, J. P.; Neiser, R. A.; Wolf, P. D. *Phys. Rev. B* **1995**, *38*, 1.
- (25) Erbil, A.; Cargill, G. S., III; Frahm, R.; Boehme, R. F. *Phys. Rev. B* **1988**, *37*, 2450.
- (26) Yoshida, T.; Tanaka, T.; Yoshida, H.; Funabiki, T.; Yoshida, S.; Murata, T. *J. Phys. Chem.* **1995**, *99*, 10890.
- (27) Yoshida, T.; Tanaka, T.; Yoshida, H.; Funabiki, T.; Yoshida, S. *J. Phys. Chem.* **1996**, *100*, 2303.
- (28) Aritani, H.; Yamada, H.; Nishio, T.; Imamura, S.; Hasegawa, S.; Tanaka, T.; Yoshida, S. *Chem. Lett.* **1999**, 359.
- (29) Murata, T.; Matsukawa, T.; Naoe, T.; Horigome, S.; Matsudo, O.; Matanabe, M. *Rev. Sci. Instrum.* **1992**, *63*, 1309.
- (30) Kinoshita, T.; Takata, Y.; Matsukawa, T.; Aritani, H.; Matsuo, S.; Yamamoto, T.; Takahashi, M.; Yoshida, H.; Yoshida, T.; Ufuktepe, Y.; Nath, K. G.; Kimura, S.; Kitajima, Y. *J. Synchrotron Rad.* **1998**, *5*, 726.
- (31) Tanaka, T.; Yamashita, H.; Tsuchitani, R.; Funabiki, T.; Yoshida, S. *J. Chem. Soc., Faraday Trans. 1* **1988**, *84*, 2987.
- (32) Bart, J. C. *Adv. Catal.* **1986**, *34*, 203.
- (33) Wong, J.; Rek, Z. U.; Rowen, M.; Tanaka, T.; Scafers, B.; Muller, G.; Georg, N.; Pickering, I. J.; Via, G.; DeVries, B.; Brown, G. E. H.; Froba, M. *Phys. B* **1995**, *208*, 220.
- (34) Nishi, K.; Shimizu, K.; Takamatsu, M.; Yoshida, H.; Satsuma, A.; Tanaka, T.; Yoshida, S.; Hattori, T. *J. Phys. Chem. B* **1998**, *102*, 10190.
- (35) Shimidzu, K.; Kato, Y.; Yoshida, T.; Yoshida, H.; Satsuma, A.; Hattori, T. *Chem. Commun.* **1999**, 1681.
- (36) Bart, J. C.; Vlaic, G. *Adv. Catal.* **1987**, *35*, 1.
- (37) Zakharenko, V. S. *Catal. Today* **1997**, *39*, 243.
- (38) Zecchina, A.; Lofthouse, M. G.; Stone, F. S. *J. Chem. Soc., Faraday Trans. 1* **1975**, *71*, 1476.
- (39) Colussia, S.; Marchese, L. *Catal. Today* **1998**, *41*, 229.
- (40) Murphy, D.; Giamello, E.; Zecchina, A. *J. Phys. Chem.* **1993**, *97*, 1739.
- (41) Zhang, Z.; Verykios, E.; Baerns, M. *Catal. Rev. Sci. Eng.* **1994**, *36*, 507.
- (42) Roos, J. A.; Korf, S. J.; Veehof, R. H. J.; van Ommen, J. G.; Ross, J. R. H. *Appl. Catal.* **1989**, *52*, 131.
- (43) Galuska, J. *Catal. Today* **1994**, *21*, 321.